Progress in PHOTOVOLTAICS

PROGRESS IN PHOTOVOLTAICS: RESEARCH AND APPLICATIONS
*Prog. Photovolt: Res. Appl.* (2017)
Published online in Wiley Online Library (wileyonlinelibrary.com). DOI: 10.1002/pip.2872

EU PVSEC PAPER

# New guidelines for a more accurate extraction of solar cells and modules key data from their current–voltage curves

Bertrand Paviet-Salomon[1]*, Jacques Levrat[1], Vahid Fakhfouri[2], Yanik Pelet[2], Nicolas Rebeaud[2], Matthieu Despeisse[1] and Christophe Ballif[1]

[1] PV-Center, CSEM, Rue Jaquet-Droz 1, Neuchâtel, CH-2002, Switzerland
[2] Meyer Burger Group, Pasan S.A., Rue Jaquet-Droz 8, Neuchâtel, CH-2000, Switzerland

## ABSTRACT

This paper investigates the optimisation of the fit procedures to determine with the highest accuracy the key data of photovoltaic cells and modules from their current–voltage characteristics. Our analysis is based on numeric current–voltage curves obtained by solving the two-diode equation in steady state. The established state-of-the-art fit procedures, such as the ASTM E948-09 standard, are shown to be outperformed by smart adjustments of the fit range and the regression type. As a result of this optimisation, the accuracy in determining the short-circuit current density is improved by up to 15 times, the open-circuit voltage by 3 to 10 times and the maximum power by 4 to 5 times, in comparison to state-of-the-art approaches. It is demonstrated that the signal-to-noise ratio of the experimental data strongly influences the fit accuracy, and therefore, the fit criteria must be adjusted according to the noise level of the measuring unit. Finally, our fit procedures were applied to experimentally measured current–voltage curves of 3000 silicon heterojunction solar cells. Notably, the established fit standards are shown to overestimate the maximum power by up to 0.2%, whereas our proposed fit yields more consistent values. In conclusion, novel fit guidelines are provided, aiming at enhancing the key data determination of high-efficiency photovoltaic cells and modules. Copyright © 2017 John Wiley & Sons, Ltd.

**KEYWORDS**

ASTM E948-09 standard; fitting; *I–V* curve; key data; polynomials; power rating; crystalline silicon; solar cell

***Correspondence**

Bertrand Paviet-Salomon, PV-Center, CSEM, Rue Jaquet-Droz 1, CH-2002 Neuchâtel, Switzerland.
E-mail: bertrand.paviet-salomon@csem.ch

Received 13 May 2016; Revised 12 January 2017; Accepted 16 January 2017

## 1. INTRODUCTION

The accurate rating of photovoltaic (PV) cells and modules under standard test conditions is an essential part of their characterisation. The key data—namely, the short-circuit current density ($J_{sc}$), the open-circuit voltage ($V_{oc}$), and the nominal peak power ($P_{mpp}$) at maximum power point (MPP)—are extracted from the measured current–voltage (*I–V*) characteristic of the device under test (DUT). Accurate key data are of fundamental importance for PV devices manufacturers and customers. Continuous improvements nowadays allow certification institutes to achieve better than 2% accuracy on key data measurements for crystalline silicon-based PV devices [1]. There exist abundant literature and international standards precisely defining the appropriate way to conduct PV devices rating, especially regarding spectrum and irradiance of the light source [2] [3] [4] [5], DUT temperature control and monitoring [2] [4] [6], contacting of the DUT [2] [7], reference cells [8] [9] [10], to name a few. In contrast, the post-processing of the *I–V* data themselves, that is, how $J_{sc}$, $V_{oc}$ and $P_{mpp}$ are actually extracted, is covered in much less extent, be it in research papers [11] [12] or in international standards [13] [7]. The only existing international standard precisely describing a procedure for the key data extraction is the ASTM E948-09 norm [13]. K. Emery from NREL suggested alternative fit ranges and procedures in [14]. Notably, neither the ASTM norm nor the NREL paper provides an estimation of the accuracy obtained following their fit guidelines. In contrast, Dirnberger and Kräling provide in [1] an exhaustive determination of the key data measurement uncertainties at Fraunhofer ISE CalLab, but the precise details regarding the key data extraction are undisclosed.

In our recent paper [15], the determination of PV cells and modules $P_{mpp}$ from their *I–V* characteristics has been investigated. Our analysis was based on synthetic *I–V* curves generated by numerically solving the two-diode equation in steady-state conditions. A broad population of synthetic *I–V* curves with different shapes and key data was generated, and the accuracy and robustness of the ASTM, the NREL and our $P_{mpp}$ fits were assessed on this device population. Frequent shortcomings of the ASTM and the NREL fits were observed, namely, an overestimation of $P_{mpp}$ up to 0.25%. A novel fit procedure has been proposed and optimised, where the fit boundaries are defined by two independent thresholds expressed as a fraction of $P_{mpp}$, and no longer based on $J_{mpp}$ and $V_{mpp}$ boundaries as advocated by the ASTM norm [13]. As a major achievement, our fit procedure resulted in 3 to 4 times more accurate values of $P_{mpp}$ than those obtained following the ASTM or the NREL guidelines. More importantly, our fit performed equally accurate regardless of the device fill factor (*FF*). In contrast, the ASTM and the NREL fits yield $P_{mpp}$ values overestimated by more than 0.1% for devices with *FF* of 78% or higher. This overestimation has been shown to be linked to an improper choice of the range where $P_{mpp}$ was fitted. The effect of the polynomial order on the fit accuracy was also investigated. Finally, our results were validated by measuring actual PV single cells and full modules. Further details can be found in [15].

This paper aims at completing our previous study by investigating in more details the fit procedures not only for $P_{mpp}$, but also for $J_{sc}$ and $V_{oc}$. The fit parameters for $J_{sc}$, $V_{oc}$ and $P_{mpp}$ are optimised, and their sensitivity to the measurement noise is discussed. The results are then compared to the ASTM and the NREL procedures. As a case study, the validity and robustness of our approach are assessed one step further by testing it on *I–V* curves experimentally measured on 3000 commercial-grade 6-in silicon heterojunction (SHJ) solar cells. The key data obtained with our fits are benchmarked against those extracted using the ASTM and the NREL guidelines, and the peculiarities of each procedure are discussed. Finally, general recommendations aiming at enhancing the accuracy of the solar cells and modules key data extraction from their *I–V* characteristics are provided.

## 2. EXPERIMENTAL

### 2.1. Synthetic *I–V* curve generation

The main points of our approach, also presented in more details in [15], are summarised in the succeeding texts. Synthetic *I–V* curves are generated using the commercial software Matlab [16]. The starting point of our approach is to numerically solve the two-diode equation in steady state, according to (1).

$$J = J_L - J_{01}\left\{\exp\left[\frac{q(V+JR_s)}{n_1kT}\right]-1\right\} - J_{02}\left\{\exp\left[\frac{q(V+JR_s)}{n_2kT}\right]-1\right\} - \frac{V+JR_s}{R_p} \quad (1)$$

In (1), $k$ is Boltzmann's constant, $T$ the DUT temperature, $J_L$ the light generated current density, $J_{01}$ and $J_{02}$ the first and second diode saturation current densities, respectively, $n_1$ and $n_2$ the associated ideality factors, $R_p$ the shunt resistance and $R_s$ the series resistance. $V$ is the input vector containing the voltage values where (1) is to be solved, and $J$ is the output vector containing the calculated current density values for each element in $V$. In all the following, we set $T$ to 298 K, $n_1$ to 1 and $n_2$ to 2. Note that we verified that the results presented in this paper and in [15] remain valid for $n_1 > 1$ and $n_2 > 2$ values. The vector $V$ takes values between $-0.5$ and 1.0 V, with a sampling frequency of 1 mV$^{-1}$. Once known $V$ and $J$, the full *I–V* curve is reconstructed. Moreover, solving the two-diode equation (1) for the specific case $V=0$ (resp. $J=0$), the theoretical value of $J_{sc}$ (resp. $V_{oc}$) is determined. Finally, the theoretical value of $P_{mpp}$ is extracted, and the *FF* is calculated. These values are named $J_{sc,th}$, $V_{oc,th}$, $P_{mpp,th}$ and $FF_{th}$, respectively. Note that the accuracy in determining the actual values of $J_{sc,th}$, $V_{oc,th}$, $P_{mpp,th}$ and $FF_{th}$ is given by the numerical accuracy of the Matlab solving algorithms and is well below $10^{-5}$%.

Applying this model, a virtual population of 500 *I–V* curves whose two-diode parameters ($J_L$, $J_{01}$, $J_{02}$, $R_s$, $R_p$) are randomly chosen into representative ranges for crystalline silicon-based solar cells is generated (see [15] and the references therein). The resulting distributions for $J_{sc,th}$, $V_{oc,th}$, $FF_{th}$ and $P_{mpp,th}$ are plotted in Figure 1.

White Gaussian noise with variance $\sigma_J$ is afterwards added to the current vector $J$ to simulate the effects of an actual measurement. The noise vector on $J$ is noted $J_{noise}(\sigma_J)$. The signal-to-noise ratio (SNR) in decibel (dB) for the current vector $J$ is then calculated as:

$$SNR_{dB} = 10\times\log_{10}\left(\frac{\overline{J^2}}{\overline{J^2_{noise}(\sigma_J)}}\right) \quad (2)$$

Similarly, the noise vector for the voltage channel ($V_{noise}(\sigma_V)$), with variance $\sigma_V$, and the corresponding SNR, are calculated. The resulting SNR as a function of $\sigma_J$ and $\sigma_V$ is plotted in Figure 2. The noised *I–V* curves under study feature a wide variety of shapes and key data and serve as basis throughout this paper to evaluate the accuracy and the robustness of the ASTM, the NREL and our fit procedures in determining the key data.

### 2.2. Fit procedures for $J_{sc}$, $V_{oc}$ and $P_{mpp}$

Table I details the fit ranges and methods used to extract $J_{sc}$, $V_{oc}$ and $P_{mpp}$, according to the ASTM and the NREL guidelines, as well as the ones proposed in [15] and further

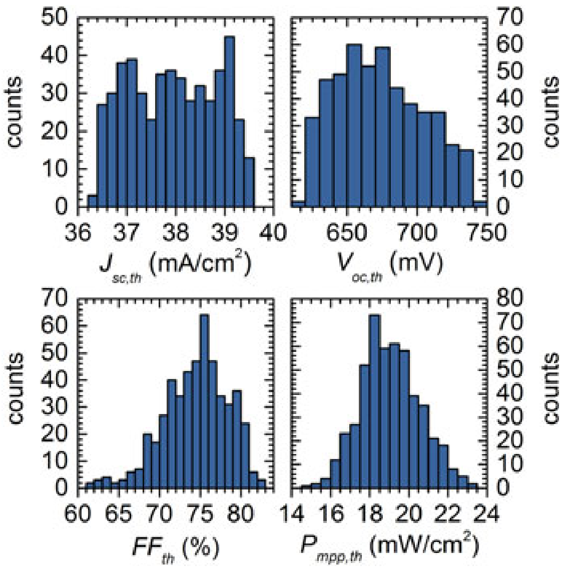


**Figure 1.** Histograms of the theoretical values of $J_{sc}$, $V_{oc}$, $FF$ and $P_{mpp}$ for the 500 synthetic *I–V* curves under study. [Colour figure can be viewed at wileyonlinelibrary.com]

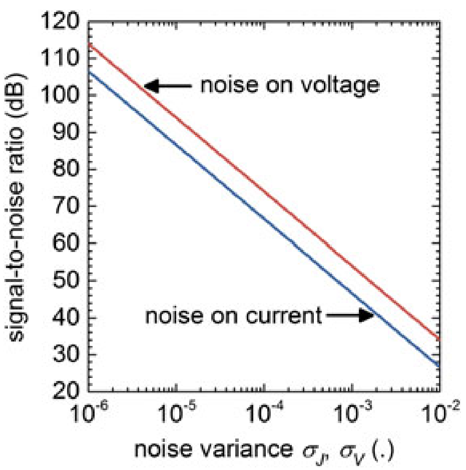


**Figure 2.** Resulting signal-to-noise ratio as a function of the noise variance. [Colour figure can be viewed at wileyonlinelibrary.com]

investigated in this paper. Each procedure is now briefly discussed and compared.

Regarding $J_{sc}$ fit, ASTM proposes the simplest approach, namely, a linear interpolation of the two ($J$, $V$) points closest to zero voltage. NREL also recommends a linear fit but includes more data points in the fit range. We propose as well to use a linear fit, but on a somewhat different voltage range, namely, $\alpha \times V_{mpp} \leq V \leq \beta \times V_{mpp}$, where $-0.5 \leq \alpha < 0$ and $0 < \beta \leq 1$.

The ASTM and the NREL guidelines for $V_{oc}$ fit are quite similar to those for $J_{sc}$: they both use a linear fit, on the two ($J$, $V$) points bracketing zero current in the case of ASTM, and on a larger range in the case of NREL. In contrast, we compare the use of a linear vs. a second-order polynomial fits, on ($J$, $V$) points fulfilling the condition $\gamma \times J_{mpp} \leq J \leq \delta \times J_{mpp}$, where $-0.25 \leq \gamma < 0$ and $0 < \delta \leq 0.5$.

In the case of $P_{mpp}$, the ASTM fit and ours use a fourth-order polynomial fit, whereas NREL recommends the use of a polynomial fit of the fourth-order *or higher*. The major differences arise regarding the fit range: indeed, the ASTM norm defines the $P_{mpp}$ fit range on ($J$, $V$) points based on $V_{mpp}$ and $J_{mpp}$ fractions. In contrast, following NREL, we define the $P_{mpp}$ fit range on ($P$, $V$) points as a function of $P_{mpp}$ fraction. However, whereas NREL uses a single $P_{mpp}$ threshold, our $P_{mpp}$ fit range is defined by two independent thresholds: $a_0 \times P_{mpp}$ for voltages smaller than $V_{mpp}$ and $b_0 \times P_{mpp}$ for voltages greater than $V_{mpp}$, where $a_0$ and $b_0$ take values between 0 and 1.

For each guideline, the extracted key data are compared to the theoretical values (determined by solving the two-diode equation, see Section 2.1), and the absolute errors are calculated according to (3).

$$\varepsilon(X) = \left| \frac{X_{fit} - X_{th}}{X_{th}} \right| \tag{3}$$

In (3), $X = J_{sc}$, $V_{oc}$, or $P_{mpp}$. The mean value and the standard deviation of $\varepsilon(X)$, calculated on the 500 *I–V* curves under study, are also reported and noted $\overline{\varepsilon}(X)$ and $\sigma(\varepsilon(X))$, respectively.

### 2.3. Actual measurements of silicon heterojunction solar cells

A total of 3000 6-in, commercial-grade SHJ solar cells were measured at our facilities using a class AAA Wacom steady-state solar simulator equipped with a Grid$^{\text{TOUCH}}$ contacting system [17] in standard test conditions at 25 °C under AM1.5G equivalent illumination. The SNR is higher than 80 dB for our experimental set-up. The measured *I–V* curves are afterwards fitted with the ASTM, the NREL and our fit procedures, as described in Table I (Section 2.2), and the key data are extracted and compared. The histograms of the short-circuit current ($I_{sc}$), $V_{oc}$, $FF$ and $P_{mpp}$ values obtained using our fit criteria are displayed in Figure 3. The SHJ devices under study are tightly distributed around mean values of $I_{sc}$ = (9.34 ± 0.06) A, $V_{oc}$ = (726 ± 5) mV, $FF$ = (79 ± 1) % and $P_{mpp}$ = (5.3 ± 0.1) W.

As the actual values of the key data are not known *a priori* for these 3000 solar cells, the differences $\Delta^{ASTM}(X)$ between the key data determined using the ASTM guidelines and those using our fit criteria are calculated following equation (4), where $X = I_{sc}$, $V_{oc}$, or $P_{mpp}$. Similarly, the differences $\Delta^{NREL}(X)$ between the NREL fits and ours are calculated.

$$\Delta^{ASTM}(X) = \frac{X^{ASTM} - X^{this\ work}}{X^{this\ work}} \tag{4}$$

**Table I.** Overview of the fit ranges and methods under study used to determine the solar cells and modules key data from their current–voltage curves.

| | Ref. Year | ASTM [13] 2009 | NREL [14] 2011 | This work 2016 |
|---|---|---|---|---|
| $J_{sc}$ fit | Type | Linear | Linear | Linear |
| | Range | Two (*J*, *V*) points closest to zero voltage | (*J*, *V*) points such that $\lvert J\rvert < 0.04 \times J_{V=0}$ $\lvert V\rvert < 0.2 \times V_{J=0}$ | (*J*, *V*) points such that $\alpha \times V_{mpp} \leq V \leq \beta \times V_{mpp}$ with $-0.5 \leq \alpha < 0$ and $0 < \beta \leq 1$ |
| $V_{oc}$ fit | Type | Linear | Linear | Linear or second-order polynomial |
| | Range | Two (*J*, *V*) points closest to zero current | (*J*, *V*) points such that $\lvert J\rvert < 0.2 \times J_{V=0}$ $\lvert V\rvert < 0.1 \times V_{J=0}$ | (*J*, *V*) points such that $\gamma \times J_{mpp} \leq J \leq \delta \times J_{mpp}$ with $-0.25 \leq \gamma < 0$ and $0 < \delta \leq 0.5$ |
| $P_{mpp}$ fit | Type | Fourth-order polynomial | ≥ Fourth-order polynomial | Fourth-order polynomial |
| | Range | (*J*, *V*) points such that: $0.75 \times V_{mpp} < V < 1.15 \times V_{mpp}$ $0.75 \times J_{mpp} < J < 1.15 \times J_{mpp}$ | (*P*, *V*) points such that: $P > 0.8 \times P_{mpp}$ $V > 0.8 \times V_{mpp}$ | (*P*, *V*) points such that $P \geq a_0 \times P_{mpp}$ for $V < V_{mpp}$ $P \geq b_0 \times P_{mpp}$ for $V \geq V_{mpp}$ with $0 < a_0, b_0 < 1$ |

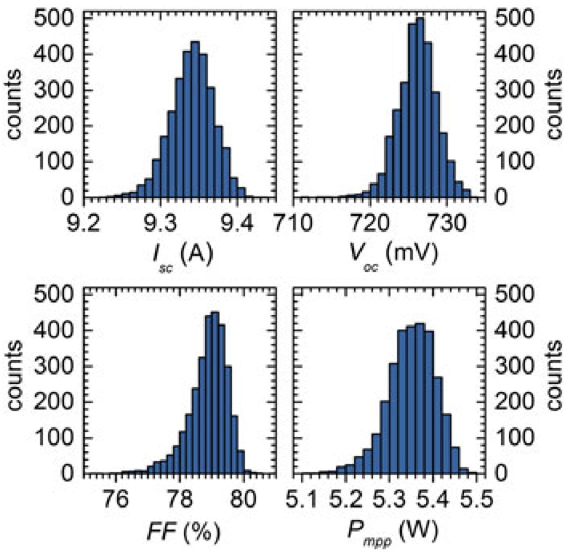


**Figure 3.** Histograms of the measured key data of 3000 6-in silicon heterojunction solar cells, determined using the fit criteria presented in this paper. [Colour figure can be viewed at wileyonlinelibrary.com]

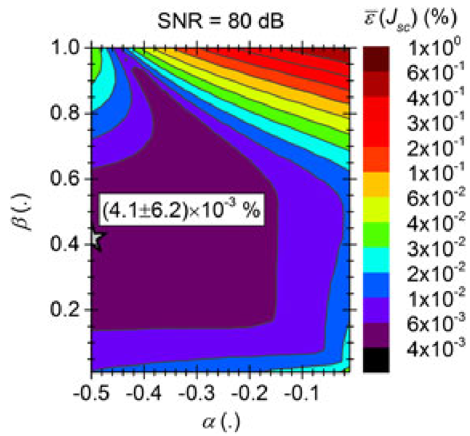


**Figure 4.** Variation of the mean absolute error on $J_{sc}$ ($\bar{\varepsilon}(J_{sc})$) as a function of the ($\alpha$, $\beta$) boundaries used for the fit range, in the case of a signal-to-noise ratio of 80 dB. The grey star indicates the position of the minimum for $\bar{\varepsilon}(J_{sc})$. [Colour figure can be viewed at wileyonlinelibrary.com]

## 3. RESULTS AND DISCUSSION

### 3.1. Short-circuit current density fit

Figure 4 plots the variation of $\bar{\varepsilon}(J_{sc})$ as a function of the ($\alpha$, $\beta$) boundaries in the case SNR = 80 dB. The minimum value of $\bar{\varepsilon}(J_{sc})$ is obtained when $\alpha = -0.50$ and $\beta = 0.42$ and equals $(4.1 \pm 6.2) \times 10^{-3}$%. Repeating this experiment for the other SNR values, the ($\alpha$, $\beta$) boundaries minimising $\bar{\varepsilon}(J_{sc})$ are determined in each case. The resulting minimum values of $\bar{\varepsilon}(J_{sc})$ are plotted in Figure 5 and compared to the values obtained with the ASTM and the NREL fits. Overall, all fits perform better for higher SNRs, that is, lower noise level. Interestingly, in the no-noise limit (corresponding to the case $SNR \to \infty$), the ASTM fit, which uses only the two data points bracketing zero voltage to determine $J_{sc}$, performs the best. Nevertheless, this approach results very sensitive to noise, as the error given by the ASTM fit rapidly grows when the SNR decreases. Indeed, $\bar{\varepsilon}(J_{sc})$ for the ASTM fit is already $7 \times 10^{-3}$% at 100 dB and up to 0.7% at 60 dB, whereas it is respectively $6 \times 10^{-4}$% and $3 \times 10^{-2}$% with our fit. The NREL fit also degrades with noise, even if its errors are for most SNRs slightly lower than with the ASTM fit. In contrast—even if also sensitive to noise—our fit yields higher accuracy than the ASTM and the NREL fits for SNRs of 100 dB and lower, thanks to its optimised fit range.

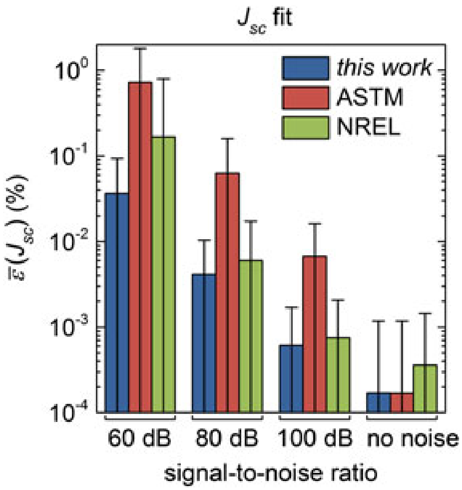


**Figure 5.** Comparison of the mean absolute error on $J_{sc}$ ($\bar{\varepsilon}(J_{sc})$) as a function of the signal-to-noise ratio. The error bars are the $2\sigma$ deviation of $\varepsilon(J_{sc})$ for the 500 solar cells under investigation. [Colour figure can be viewed at wileyonlinelibrary.com]

## 3.2. Open-circuit voltage fit

Following the same approach applied for $J_{sc}$ fit (Section 3.1), the ($\gamma$, $\delta$) boundaries minimising $\bar{\varepsilon}(V_{oc})$ are determined for each SNR values, in the case of a linear regression and a second-order polynomial fit. The results in the case SNR = 80 dB are exemplary plotted in Figure 6. As can be seen, for this SNR value, the minimum values of $\bar{\varepsilon}(V_{oc})$ obtained with the linear or the second-order polynomial fits are quite similar: $(4.5 \pm 6.9) \times 10^{-3}$% for the former and $(3.6 \pm 5.4) \times 10^{-3}$% for the latter. However, the two fits behave significantly differently as a function of the ($\gamma$, $\delta$) boundaries. Indeed, in the case of the linear fit, the ($\gamma$, $\delta$) zone yielding the lowest $\bar{\varepsilon}(V_{oc})$ values is sharply delimited, and $\bar{\varepsilon}(V_{oc})$ rapidly grows outside this region, reaching up to $10^{-1}$% error. In contrast, the second-order polynomial fit yields $\bar{\varepsilon}(V_{oc})$ values not higher than $10^{-2}$% regardless of the chosen boundaries. This suggests a higher robustness of the second-order polynomial fit regarding the chosen fit range.

Figure 7 compares the performances of our $V_{oc}$ fit (linear and second-order polynomial) to the ASTM and the NREL ones (which both use a linear regression). Interestingly, among the linear fits, the simple two-point linear fit of ASTM performs the best in the no-noise limit. Nonetheless, for SNRs of 100 dB and lower, our optimised linear fit yields higher accuracy. Note that the NREL fit usually gives higher errors than ASTM and our work, but is remarkably insensitive to noise. Moreover, it was found

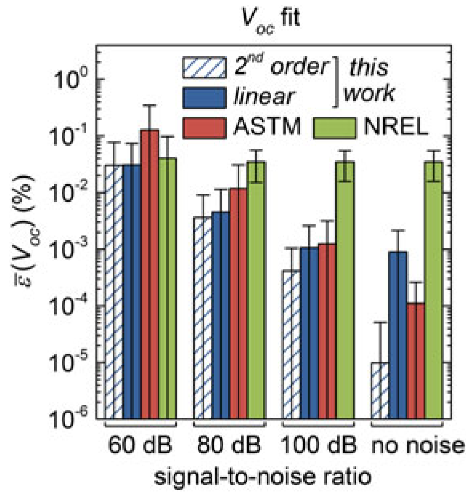


**Figure 7.** Comparison of the mean absolute error on $V_{oc}$ ($\bar{\varepsilon}(V_{oc})$) as a function of the signal-to-noise ratio. The error bars are the $2\sigma$ deviation of $\varepsilon(V_{oc})$ for the 500 solar cells under investigation. [Colour figure can be viewed at wileyonlinelibrary.com]

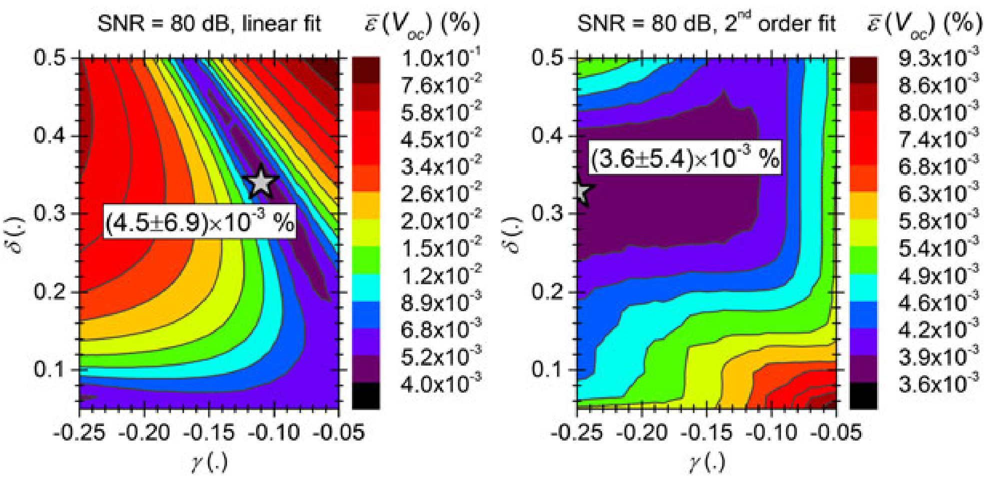


**Figure 6.** Variation of the mean absolute error on $V_{oc}$ ($\bar{\varepsilon}(V_{oc})$) as a function of the ($\gamma$, $\delta$) boundaries used for the fit range, in the case of a signal-to-noise ratio of 80 dB, using a linear regression (left) and a second-order polynomial fit (right). The grey stars indicate the position of the minimum for $\bar{\varepsilon}(V_{oc})$. [Colour figure can be viewed at wileyonlinelibrary.com]

that the NREL fit procedure mainly yields underestimated $V_{oc}$ values. This topic is addressed in more details at the end of this section.

Using a second-order polynomial fit as an alternative to the standard linear regression, the most accurate values of all benchmarked fits are obtained, even in the no-noise limit (see the blue hatched bars in Figure 7). One possible explanation for the superior results of the second-order polynomial fit compared to the linear regression is that the former better accommodates to the curvature of the *I–V* curve close to $V_{oc}$. However, as seen in Figure 7, the superiority of the second-order polynomial fit rapidly reduces when noise increases. Indeed, whereas in the no-noise case, the second-order polynomial fit is almost two orders of magnitude more accurate than the linear one, this improvement drops to only 3 times at SNR = 100 dB. At 80 dB, the accuracy gain of the second-order polynomial fit is marginal, and at 60 dB, it performs similarly to the

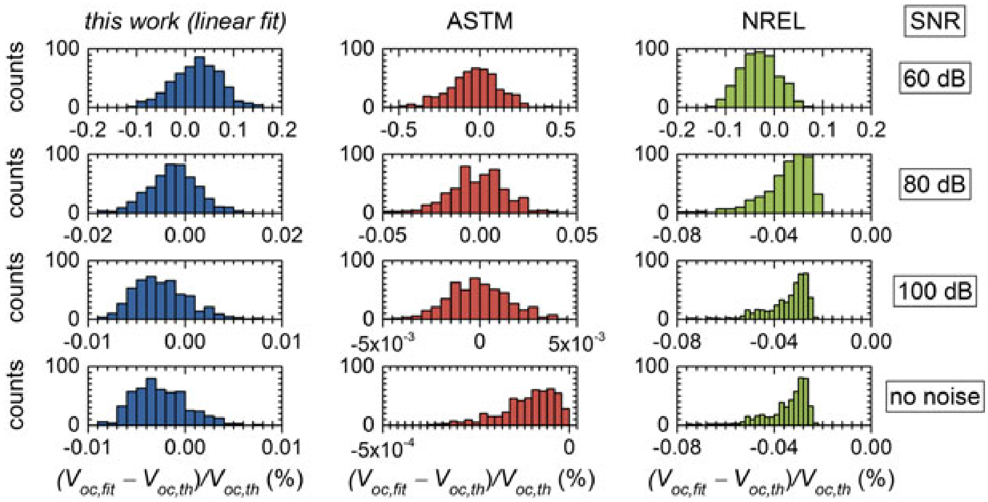


**Figure 8.** Histograms of the signed error on $V_{oc}$ ($(V_{oc,fit} - V_{oc,th})/V_{oc,th}$) as a function of the signal-to-noise ratio. [Colour figure can be viewed at wileyonlinelibrary.com]

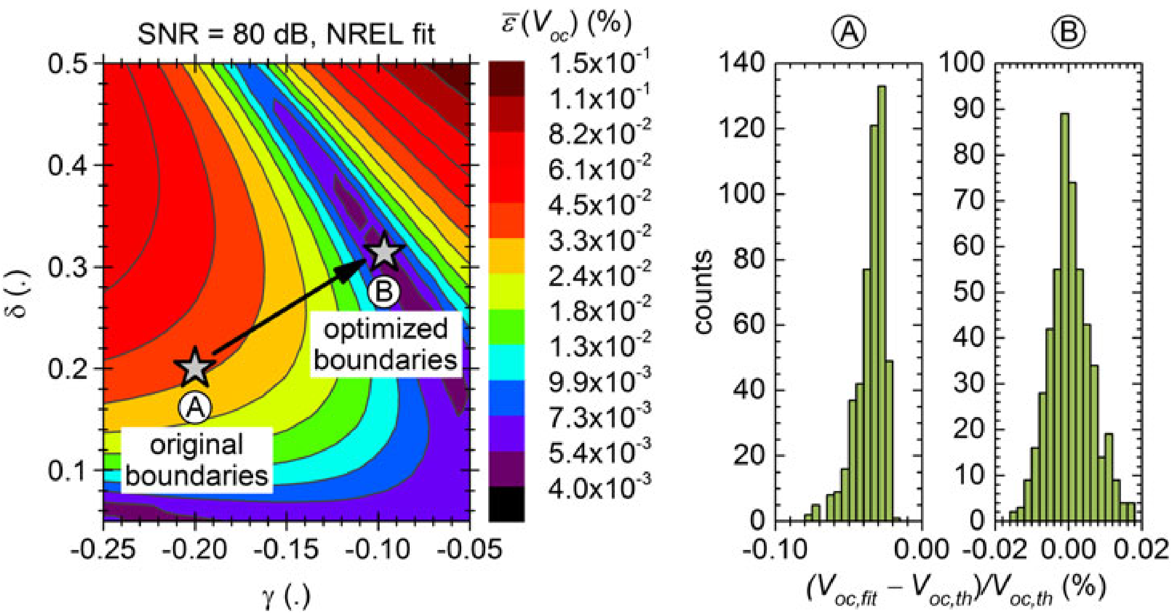


**Figure 9.** Illustration of the fit range influence on the systematic error in determining the $V_{oc}$ with the NREL fit. Using the original NREL boundaries yields a mean absolute error on $V_{oc}$ of (3.5 ± 2.0) × $10^{-2}$% together with a systematic underestimation of the actual $V_{oc}$ value (see the 'A' histogram featuring only negative values). In contrast, the optimised boundaries allow reducing the mean absolute error to (4.5 ± 7.2) × $10^{-3}$% with no systematic error (see the 'B' histogram evenly distributed around zero). [Colour figure can be viewed at wileyonlinelibrary.com]

linear regression. Last but not least, using a second-order polynomial fit for $V_{oc}$ determination does not go without new challenges. Indeed, second-order polynomials usually have two roots: determining which one actually is the 'true' value of $V_{oc}$ can reveal quite delicate. A first approach would be to compare the two $V_{oc}$ roots of the second-order polynomial to the $V_{oc}$ value obtained using the linear regression: the one of the two roots closest to this latter value might be assumed to be a more accurate estimation of the actual $V_{oc}$. Further investigations are however needed to fully assess the validity of this approach.

Figure 8 plots the histograms of the signed error on $V_{oc}$ (calculated as $(V_{oc,fit} - V_{oc,th})/V_{oc,th}$) obtained with the ASTM, the NREL and our linear fit for all SNRs. In contrast to $\varepsilon(V_{oc})$ (see (3) in Section 2.2), which is always positive, the signed error on $V_{oc}$ can take positive or negative values: a positive value indicates an overestimation of the actual $V_{oc}$, whereas a negative value indicates an underestimated $V_{oc}$. As can be seen in Figure 8, for all SNRs but 60 dB, the histograms of the signed error on $V_{oc}$ of the NREL fit take only negative values. This indicates that the $V_{oc}$ determined using the NREL procedure is lower than the actual one, as already briefly mentioned in the discussion of Figure 7. In contrast, the histograms of the ASTM fit and our linear fit are evenly distributed around zero, indicating no systematic deviation in their $V_{oc}$ estimation. (A notable exception is however the ASTM fit in the no-noise limit.)

As NREL uses a linear regression similarly to our $V_{oc}$ fit procedure, we can hence affirm that the peculiar behaviour

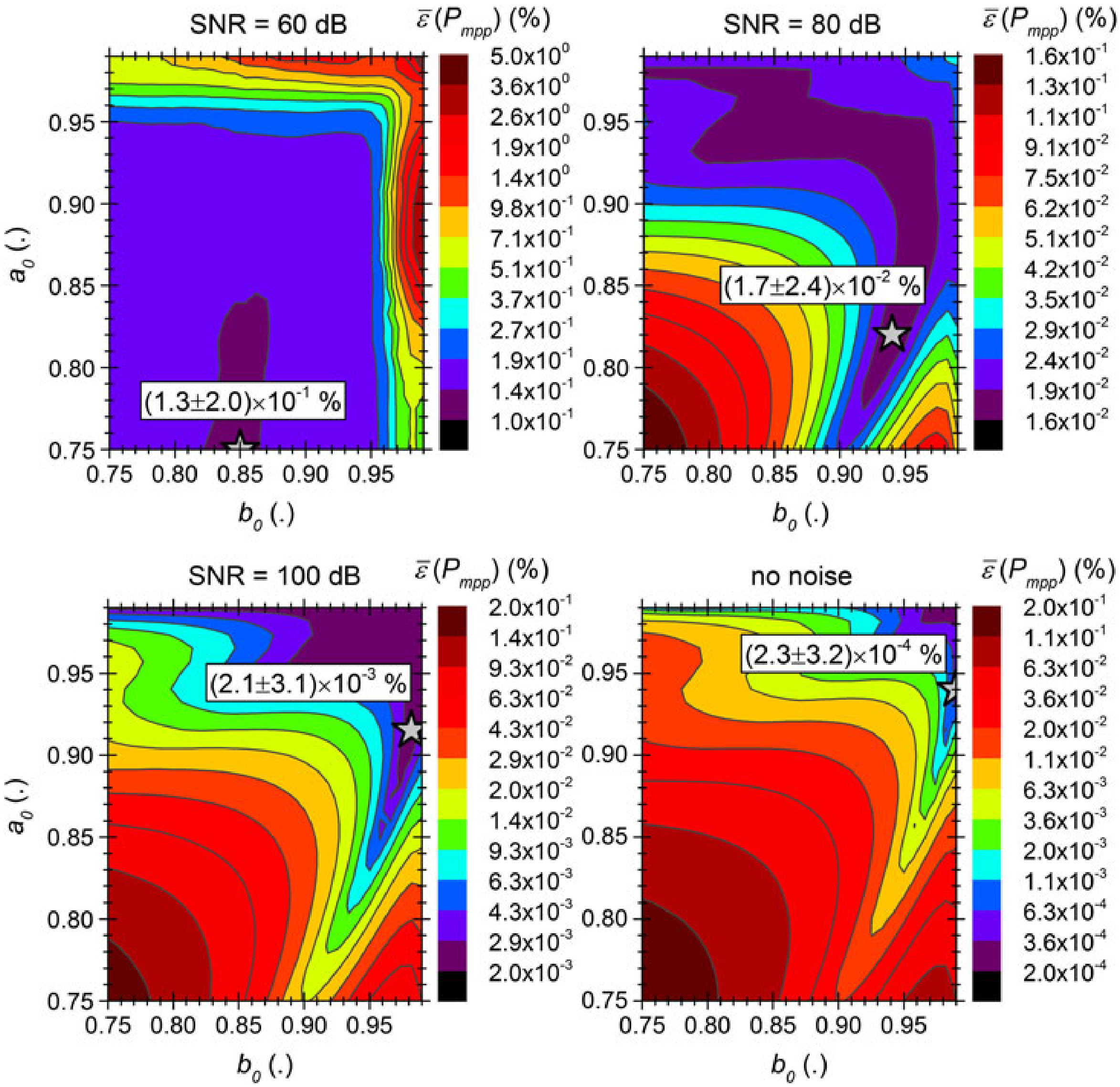


**Figure 10.** Variation of the mean absolute error on $P_{mpp}$ $(\bar{\varepsilon}(P_{mpp}))$ as a function of the ($a_0$, $b_0$) boundaries used for the fit range, for three signal-to-noise ratios and in the no-noise limit. The grey stars indicate the position of the minimum for $\bar{\varepsilon}(P_{mpp})$. [Colour figure can be viewed at wileyonlinelibrary.com]

of the NREL fit rather originates from a non-optimised choice of the fit boundaries. To illustrate this point, the NREL $V_{oc}$ fit boundaries were redefined in a similar fashion to our fit, namely, as ($J$, $V$) points fulfilling the condition $\gamma \times J_{V=0} \leq J \leq \delta \times J_{V=0}$ (where $-0.25 \leq \gamma < 0$ and $0 < \delta \leq 0.5$), still keeping the additional condition $|V| \leq 0.1 \times V_{J=0}$. The original NREL fit is then retrieved using $\gamma = -0.20$ and $\delta = 0.20$ (see Table I). The value of $\bar{\varepsilon}(V_{oc})$ is then calculated for all ($\gamma$, $\delta$) values. The results are plotted in Figure 9 in the case SNR = 80 dB. The colour map is very similar to the one obtained with our linear fit (see Figure 6, left). This was expected, as the NREL fit boundaries are now almost identical to ours. However, the map clearly reveals that the original NREL boundaries ($\gamma = -0.20$ and $\delta = 0.20$) can be advantageously replaced by the values $\gamma = -0.10$ and $\delta = 0.31$: doing so, $\bar{\varepsilon}(V_{oc})$ is reduced from $(3.5 \pm 2.0) \times 10^{-2}\%$ to $(4.5 \pm 7.2) \times 10^{-3}\%$ (compare the 'A' and 'B' grey stars on the map). Moreover, comparing the histograms of the signed error on $V_{oc}$ obtained for conditions 'A' and 'B' shows that when using the original boundaries, the histogram features only negative values, indicating underestimated $V_{oc}$ values, as already observed in Figure 8. In contrast, with the optimised boundaries, the histogram is evenly distributed around zero, indicating that any systematic error in the $V_{oc}$ determination has been cancelled. We can hence conclude that the original NREL $V_{oc}$ fit suffers from an improper fit range, resulting in a systematic error (here an underestimation) in the value of the fitted parameter.

### 3.3. Maximum power fit

Figure 10 plots the variation of $\bar{\varepsilon}(P_{mpp})$ as a function of the ($a_0$, $b_0$) boundaries for three different SNRs and in the no-noise limit. It is worth observing that both the minimum value of $\bar{\varepsilon}(P_{mpp})$ and its position change with the noise level: the lower the noise, the lower $\bar{\varepsilon}(P_{mpp})$ and the narrower the optimum ($a_0$, $b_0$) range. For instance, at 60 dB, the minimum value of $\bar{\varepsilon}(P_{mpp})$ is not lower than $(1.3 \pm 2.0) \times 10^{-1}\%$ and requires $a_0 = 0.75$ and $b_0 = 0.85$. In contrast, in the no-noise case, $\bar{\varepsilon}(P_{mpp})$ is as low as $(2.3 \pm 3.2) \times 10^{-4}\%$ and a much narrower fit range has to be used, namely, $a_0 = 0.94$ and $b_0 = 0.99$. Conversely, using a too narrow fit range with low SNR can yield strongly inaccurate $P_{mpp}$ values: if for instance one uses the no-noise fit range in the case SNR = 60 dB, $\bar{\varepsilon}(P_{mpp})$ would reach $1.9 \pm 2.5\%$, a value 10 times worse than what would be obtained using the ASTM fit.

The accuracies on $P_{mpp}$ determination for the fit procedures under investigation are reported in Figure 11. Our optimised fit performs better than the ASTM and the NREL ones regardless of the noise level. In the no-noise limit, our fit is even more than two orders of magnitude more accurate than the ASTM and the NREL ones. In

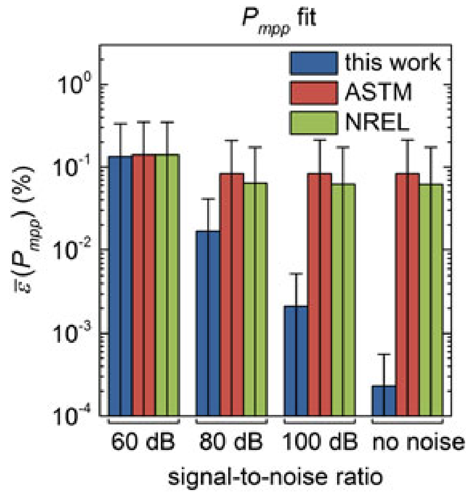


**Figure 11.** Comparison of the mean absolute error on $P_{mpp}$ ($\bar{\varepsilon}(P_{mpp})$) as a function of the signal-to-noise ratio. The error bars are the $2\sigma$ deviation of $\varepsilon(P_{mpp})$ for the 500 solar cells under investigation. [Colour figure can be viewed at wileyonlinelibrary.com]

[15], it has already been demonstrated that the main reason for the ASTM and the NREL $P_{mpp}$ fits inaccuracy originates in their too large fit range, usually leading to overestimated $P_{mpp}$ values. Moreover, it was highlighted that the $P_{mpp}$ overestimation increased with the *FF* of the DUT. At that time however, this phenomenon was investigated for a single SNR value equal to 80 dB. Figure 12 completes this study by plotting the variation of $\varepsilon(P_{mpp})$ for various SNRs. As can be seen, the ASTM and the NREL fits exhibit a marked *FF* dependency for all SNRs higher than 80 dB: the higher the DUT *FF*, the higher $\varepsilon(P_{mpp})$. Moreover, the higher the SNR, the more visible this dependency: compare, for example, the data at SNR = 80 dB with those in the no-noise limit. In contrast, when using our fit procedure, no correlation is visible between $\varepsilon(P_{mpp})$ and the DUT *FF*: our fit performs equally well for DUT with *FF* of 60% or 80%.

The results obtained in this section as a function of the SNR complete the outcomes of [15], showing (i) the $P_{mpp}$ fit range must be adapted to the ambient noise level, a rule of thumb being that high SNRs allow a narrow fit range with improved accuracy, and (ii) for a given SNR, the $P_{mpp}$ fit accuracy can be strongly dependent on the DUT *FF* if a non-optimised fit procedure is used, as was evidenced for the ASTM or the NREL ones. In contrast, our $P_{mpp}$ fit procedure proves robust against noise level and DUT *FF* variation. Guidelines detailing the appropriate $P_{mpp}$ fit parameters are provided in Table II, Section 3.5.

### 3.4. Case study: key data measurement of 3000 silicon heterojunction solar cells

Figure 13 plots the differences in determining the key data of the 3000 SHJ solar cells with the fits under study. The ASTM and the NREL fits were performed as described in Table I. For our fits, the parameters yielding the highest

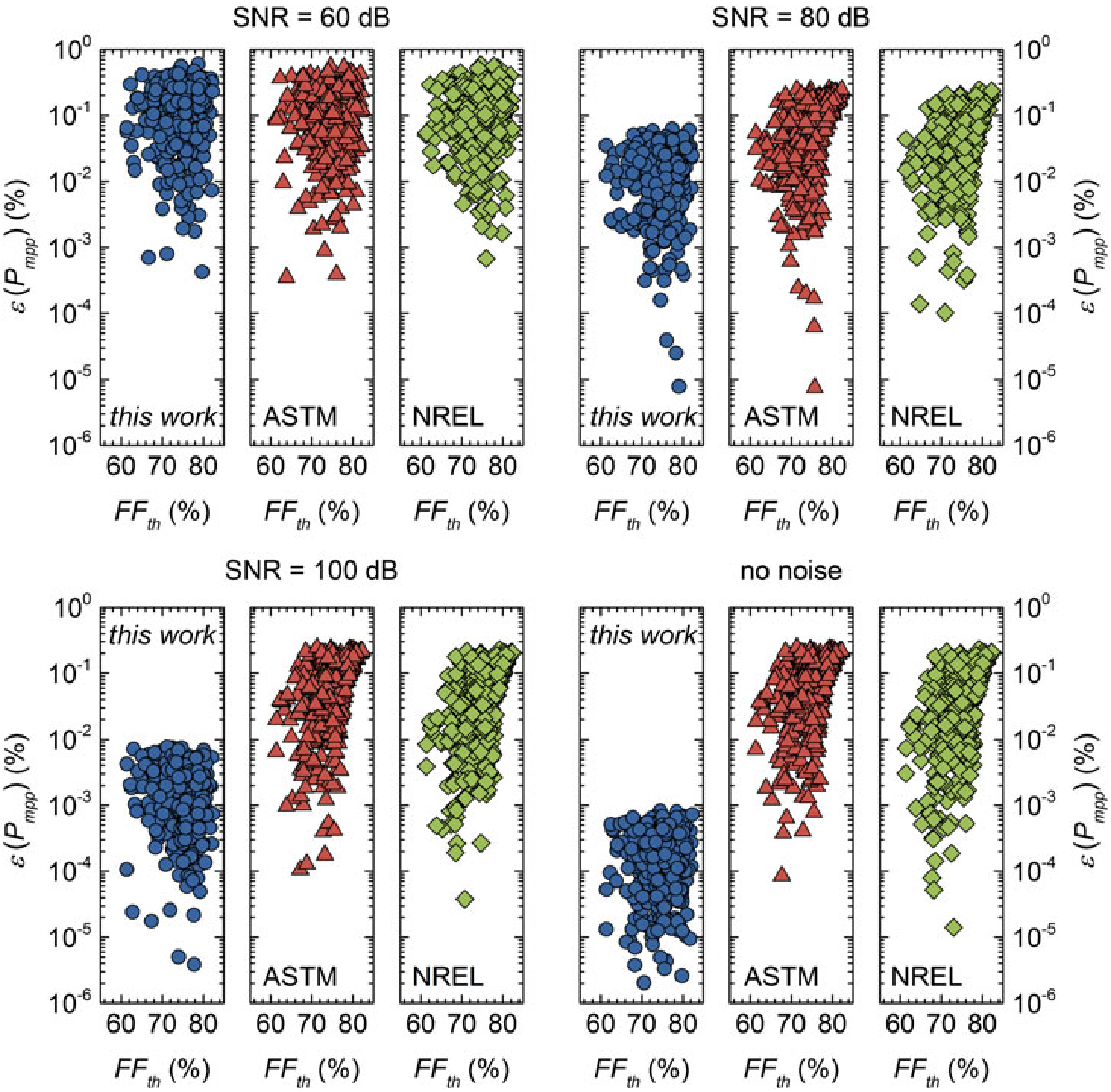


**Figure 12.** Variation of the absolute error on $P_{mpp}$ ($\varepsilon(P_{mpp})$) as a function of the theoretical *FF* of the device under test, for three signal-to-noise ratios and in the no-noise limit. Each data point represents one single *I–V* curve within the 500 under study. [Colour figure can be viewed at wileyonlinelibrary.com]

accuracy according to the results of Sections 3.1 to 3.3 were used, namely, a linear $I_{sc}$ fit on the range $-0.50 \times V_{mpp} \leq V \leq 0.42 \times V_{mpp}$, a second-order polynomial $V_{oc}$ fit on the range $-0.25 \times I_{mpp} \leq I \leq 0.33 \times I_{mpp}$ and a fourth-order polynomial $P_{mpp}$ fit using $a_0 = 0.82$ and $b_0 = 0.94$. Note that all $\Delta^{ASTM}(X)$ and $\Delta^{NREL}(X)$ values discussed in the succeeding texts in this section are larger than the typical errors expected from the calculations on synthetic *I–V* curves (Sections 3.1 to 3.3) for the signal-to-noise ratio of our experimental set-up (>80 dB) and can hence be considered meaningful.

Looking first at $I_{sc}$ fits, it is to be seen that the medians of $\Delta^{ASTM}(I_{sc})$ and $\Delta^{NREL}(I_{sc})$ are very close to zero. This means that there is no systematic deviation between these fits and ours, but rather random differences. Moreover, the $2\sigma$ deviation of $\Delta^{ASTM}(I_{sc})$ is approximately 4 times larger than those of $\Delta^{NREL}(I_{sc})$. This is consistent with the results of Figure 5: indeed, at SNR = 80 dB, the NREL fit and ours yield similar accuracy, whereas the ASTM fit was found to be less accurate. Overall, the differences between our fit and the ASTM one go up to ±0.8%, whereas it is only ±0.2% when compared to NREL.

Different behaviours are observed for $\Delta(V_{oc})$. The median of $\Delta^{ASTM}(V_{oc})$ are again close to zero, indicating random differences between our $V_{oc}$ fit and the ASTM one. In contrast, the median value of $\Delta^{NREL}(V_{oc})$ is negative: this indicates that the $V_{oc}$ values determined using the NREL procedure are systematically lower than with ours. This is

**Table II.** Fit types and ranges to be applied for the determination of crystalline silicon-based PV devices key data.

| SNR | Parameter | Fit type | Fit range | Expected error (%) |
|---|---|---|---|---|
| 60 dB | $J_{sc}$ | Linear | $-0.50 \times V_{mpp} \leq V \leq 0.55 \times V_{mpp}$ | $(3.7 \pm 5.7) \times 10^{-2}$ |
| | $V_{oc}$ | Linear | $-0.20 \times J_{mpp} \leq J \leq 0.50 \times J_{mpp}$ | $(3.1 \pm 4.3) \times 10^{-2}$ |
| | | Second-order polynomial | $-0.25 \times J_{mpp} \leq J \leq 0.50 \times J_{mpp}$ | $(3.0 \pm 4.6) \times 10^{-2}$ |
| | $P_{mpp}$ | Fourth-order polynomial | $P \geq 0.75 \times P_{mpp}$ for $V < V_{mpp}$<br>$P \geq 0.85 \times P_{mpp}$ for $V \geq V_{mpp}$ | $(1.3 \pm 2.0) \times 10^{-1}$ |
| 80 dB | $J_{sc}$ | Linear | $-0.50 \times V_{mpp} \leq V \leq 0.42 \times V_{mpp}$ | $(4.1 \pm 6.2) \times 10^{-3}$ |
| | $V_{oc}$ | Linear | $-0.11 \times J_{mpp} \leq J \leq 0.34 \times J_{mpp}$ | $(4.5 \pm 6.9) \times 10^{-3}$ |
| | | Second-order polynomial | $-0.25 \times J_{mpp} \leq J \leq 0.33 \times J_{mpp}$ | $(3.6 \pm 5.4) \times 10^{-3}$ |
| | $P_{mpp}$ | Fourth-order polynomial | $P \geq 0.82 \times P_{mpp}$ for $V < V_{mpp}$<br>$P \geq 0.94 \times P_{mpp}$ for $V \geq V_{mpp}$ | $(1.7 \pm 2.4) \times 10^{-2}$ |
| 100 dB | $J_{sc}$ | Linear | $-0.31 \times V_{mpp} \leq V \leq 0.73 \times V_{mpp}$ | $(6.1 \pm 10.8) \times 10^{-4}$ |
| | $V_{oc}$ | Linear | $-0.20 \times J_{mpp} \leq J \leq 0.05 \times J_{mpp}$ | $(1.1 \pm 1.5) \times 10^{-3}$ |
| | | Second-order polynomial | $-0.25 \times J_{mpp} \leq J \leq 0.24 \times J_{mpp}$ | $(4.2 \pm 6.3) \times 10^{-4}$ |
| | $P_{mpp}$ | Fourth-order polynomial | $P \geq 0.92 \times P_{mpp}$ for $V < V_{mpp}$<br>$P \geq 0.98 \times P_{mpp}$ for $V \geq V_{mpp}$ | $(2.1 \pm 3.2) \times 10^{-3}$ |
| No noise | $J_{sc}$ | Linear | $-0.04 \times V_{mpp} \leq V \leq 0.01 \times V_{mpp}$ | $(1.7 \pm 10.1) \times 10^{-4}$ |
| | $V_{oc}$ | Linear | $-0.20 \times J_{mpp} \leq J \leq 0.05 \times J_{mpp}$ | $(9.0 \pm 12.3) \times 10^{-4}$ |
| | | Second-order polynomial | $-0.05 \times J_{mpp} \leq J \leq 0.05 \times J_{mpp}$ | $(9.9 \pm 41.5) \times 10^{-6}$ |
| | $P_{mpp}$ | Fourth-order polynomial | $P \geq 0.94 \times P_{mpp}$ for $V < V_{mpp}$<br>$P \geq 0.99 \times P_{mpp}$ for $V \geq V_{mpp}$ | $(2.3 \pm 3.2) \times 10^{-4}$ |

PV, photovoltaic; SNR, signal-to-noise ratio.

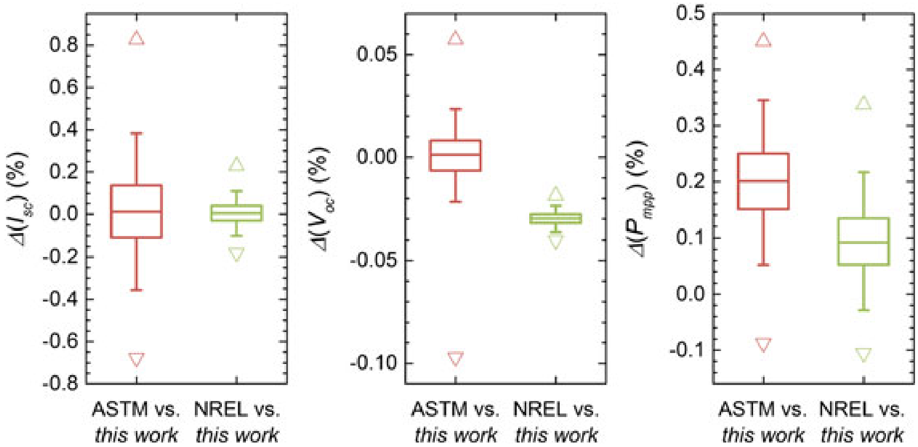


**Figure 13.** Boxplots of the differences between the key data determined using the ASTM and the NREL fits procedures against ours, in the case of 3000 silicon heterojunction solar cells. The boxes give the 25%, 50% and 75% percentiles; the whiskers are the $2\sigma$ deviations; the upward triangles give the maxima and the downward triangles the minima. [Colour figure can be viewed at wileyonlinelibrary.com]

consistent with the outcomes of Section 3.2, where it was evidenced that the NREL fit underestimates the actual $V_{oc}$ values. This difference is however less than −0.05%.

Regarding $P_{mpp}$ fit, the median values of $\Delta^{ASTM}(P_{mpp})$ and $\Delta^{NREL}(P_{mpp})$ are of 0.2% and 0.1%, respectively. This suggests that the ASTM and the NREL fits overestimate the actual $P_{mpp}$ value of the 3000 SHJ solar cells under study by these same figures. These values are in line with the outcomes of our investigations on synthetic *I–V* curves with *FF* of 78–80% presented herein in Section 3.3 and in [15], which clearly point towards an overestimation of the actual $P_{mpp}$ with the ASTM and the NREL fits, owing to their non-optimal fit ranges. The origins of this behaviour are thoroughly unveiled in [15], to which the reader is referred for further details.

Figure 14 plots $\Delta^{ASTM}(P_{mpp})$ and $\Delta^{NREL}(P_{mpp})$ as a function of the SHJ solar cells measured *FF*. For an easier interpretation of the data, the mean values of $\Delta^{ASTM}(P_{mpp})$ and $\Delta^{NREL}(P_{mpp})$ were calculated on *FF* ranges of $1\%_{abs}$ width, for example, 76–77%, and similarly up to the 80–81%

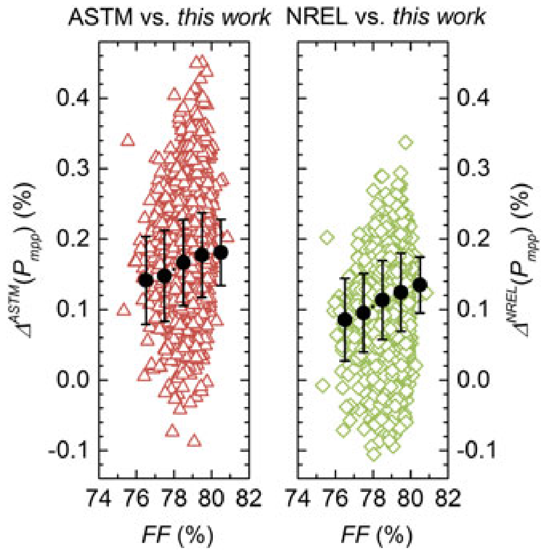


**Figure 14.** Variation of the differences between the $P_{mpp}$ values determined using the ASTM and the NREL fit procedures against ours, as a function of the *FF* of the 3000 silicon heterojunction solar cells under study. Each open triangle and diamond represents one individual device. The black dots are the mean values of $\Delta(P_{mpp})$ calculated by increment of 1$\%_{abs}$ *FF*, and the error bars are the corresponding standard deviation values. [Colour figure can be viewed at wileyonlinelibrary.com]

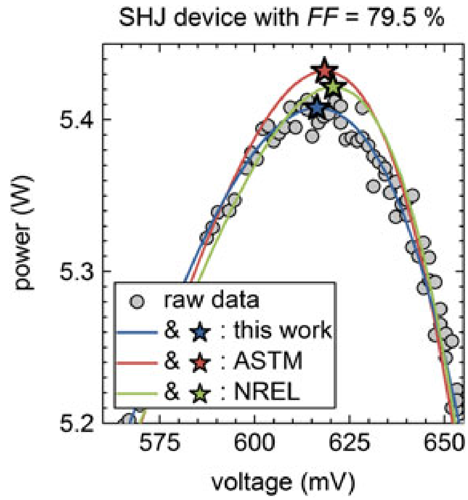


**Figure 15.** Comparison of the polynomial fits (solid lines) and the maximum power points (stars) obtained using the $P_{mpp}$ fit criteria proposed in this paper, compared to those given by ASTM [13] and NREL [14], in the case of the experimentally measured *P–V* curve of a 6-in silicon heterojunction solar cell with *FF* = 79.5%. [Colour figure can be viewed at wileyonlinelibrary.com]

range. These values are plotted as black dots in Figure 14. As can be seen, the mean values of $\Delta^{ASTM}(P_{mpp})$ and $\Delta^{NREL}(P_{mpp})$ get higher for higher *FF*. This is again consistent with the observations reported in Section 3.3 and in [15] on synthetic *I–V* curves: the higher the device *FF*, the larger the $P_{mpp}$ overestimation of the ASTM and the NREL fits. This is further confirmed by Figure 15, where the *P–V* curve of a SHJ device with *FF* = 79.5% is displayed. As can be seen, the ASTM and the NREL fits obviously overestimate the position of $P_{mpp}$, whereas our fit procedure yields a $P_{mpp}$ value better in line with the experimental data.

### 3.5. Recommendations for accurate fits

The results presented in this paper show that for $J_{sc}$, $V_{oc}$ and $P_{mpp}$ extraction, the state-of-the-art ASTM and NREL fit procedures can most of the time be outperformed by thorough adjustments of the fit range and the regression type (e.g. linear vs. second-order polynomial). This conclusion holds for *I–V* curves featuring a wide variety of shapes and key data, as well as for noise levels typically encountered in laboratory or production environments. Gathering the outcomes of the present paper and those of our previous paper [15], we provide the following recommendations to perform accurate key data extraction:

- *$J_{sc}$ fit:* Including points with negative voltage in the $J_{sc}$ fit range enhances the accuracy and robustness of the fit. For instance, at SNR = 80 dB, the expected error of our fit is $4 \times 10^{-3}$%. This represents a 15-fold (resp. 1.5-fold) accuracy improvement compared to the ASTM (resp. NREL) fit. However, this approach will obviously fail if nonlinear effects affect the negative voltage range of the *I–V* curve. Whereas this is unlikely to happen when measuring a single solar cell, in the case of PV modules, several nonlinear effects are known to appear close to $J_{sc}$, especially those linked to bypass diodes, or if a passive load is used. This problem was already pointed out in [11,14]. Adapting the $J_{sc}$ fit procedure taking into account these parasitic effects requires further investigations and is out of the scope of this paper.
- *$V_{oc}$ fit:* Similarly to $J_{sc}$, including points with negative current within the $V_{oc}$ fit range yields a better accuracy. Our linear fit with optimised boundaries provides a threefold (respectively eightfold) accuracy improvement compared to ASTM (resp. NREL) at SNR = 80 dB. Alternatively, replacing the linear regression by a second-order polynomial fit further enhances the fit performances, especially in the case of low noise environments. For instance, at SNR = 100 dB, using our second-order polynomial $V_{oc}$ fit improves the accuracy by almost two orders of magnitude compared to NREL. Nevertheless, as for $J_{sc}$, these fit procedures might result problematic for some PV modules, for example, those including blocking diodes [11]. Further investigations are also needed to address this issue, but are as well out of the scope of this paper.
- *$P_{mpp}$ fit:* Re-defining the $P_{mpp}$ fit range using two independent boundaries expressed as a fraction of $P_{mpp}$

already provides an important accuracy enhancement. At 80 dB, our fit is 5 times more accurate than ASTM, and 4 times than NREL. Even better, this fit range can itself be adapted to the *FF* of the DUT, as suggested in [15]. Even if primarily developed for single solar cells, our $P_{mpp}$ fit procedure should also be relevant in the case of full PV modules, provided that the transient effects linked to the measurement of capacitive modules are thoroughly corrected [18] [19].

- *Noise level:* The ASTM guidelines give accurate key data in the case of ideal measurements without any noise, but rapidly fail as the SNR decreases. In contrast, adapting the fit range to the SNR allows a robust and more accurate key data determination. A careful evaluation of the ambient noise is therefore a prerequisite to perform accurate fits.

Finally, Table II summarises the fit types and ranges to be used for crystalline silicon-based PV devices in order to obtain accurate key data based on the outcomes of this paper.

As a final outlook, the generalisation of our fit guidelines to other established or emerging PV technologies remains an open question. Indeed, whereas the two-diode model is widely accepted for crystalline silicon-based PV devices, numerous deviations to this simple model have been observed for other PV materials, such as copper indium gallium selenide (CIGS) [20], thin-film amorphous silicon [21] and perovskite [22]. How the key data fit guidelines have to be consequently modified requires further investigation.

## 4. CONCLUSION

In this paper, we reported on the optimisation of the fit procedures to extract crystalline silicon-based solar cells and modules key data from their *I–V* curves. Our analysis is based on numeric *I–V* curves obtained by solving the two-diode equation in steady state. Smart adjustments of the fit range and the regression type were shown to allow obtaining $J_{sc}$, $V_{oc}$ and $P_{mpp}$ values more accurately than following the established state-of-the-art standards. Our fit criteria were demonstrated to be robust against noise. The validity of our approach was assessed on *I–V* curves experimentally measured on 3000 SHJ devices. Finally, we provide novel fit criteria and general requirements aiming at enhancing the key data determination accuracy for high-efficiency crystalline silicon-based PV devices.

## REFERENCES


1. Dirnberger D, Kräling U. Uncertainty in PV module measurement—part I: calibration of crystalline and thin-film modules. *IEEE Journal of Photovoltaics* 2013; **3**(3): 1016–1026.
2. Monokroussos C, Etienne D, Morita K, Fakhfouri V, Bai J, Dreier D, Therhaag U, Herrmann W. Impact of calibration methodology into the power rating of c-Si PV modules under industrial conditions. *Proceedings of the 28th European Photovoltaic Solar Energy Conference* 2013; 2926–2934.
3. Monokroussos C, Bliss M, Qiu YN, Hibberd CJ, Betts TR, Tiwari AN, Gottschalg R. Effects of spectrum on the power rating of amorphous silicon photovoltaic devices. *Progress in Photovoltaics: Research and Applications* 2011; **19**: 640–648
4. Fakhfouri V, Herrmann W, Zaaiman W, Dreier C, Droz C, Morita K, Johnson L. Uncertainty assessment of PV power measurement in industrial environments. *Proceedings of the 26th European Photovoltaic Solar Energy Conference* 2011; 3408–3412.
5. Photovoltaic devices—part 9: solar simulator performance requirements. *IEC standard 60904-9*, *Ed.2* 2007.
6. Photovoltaic devices—part 5: determination of the equivalent cell temperature (ECT) of photovoltaic (PV) devices by the open-circuit voltage method. *IEC standard 60904-5, Ed.2* 2009.
7. Photovoltaic devices—part 1: measurement of photovoltaic current–voltage characteristics. *IEC standard 60904-1, Ed.2* 2006.
8. Winter S, Fey T, Kröger I, Friedrich D, Ladner K, Ortel B, Pendsa S, Schlüssel D. Laser-DSR facility at PTB: realization of a next generation high accuracy primary calibration facility. *Proceedings of the 27th European Photovoltaic Solar Energy Conference* 2012; 3049–3051.
9. López-Escalante MC, Fernandez MC, Sierras R, Ramos-Barrado JR. Industrial solar cell tester: study and improvement of I–V curves and analysis of the measurement uncertainty. *Progress in Photovoltaics: Research and Applications* 2016; **24**: 108–121.
10. Photovoltaic devices—part 2: requirements for reference solar devices. *IEC 60904-2, Ed.2* 2006.
11. Qasem H, Betts TR, Sara ID, Bliss M, Zhu J, Gottschalg R. Analysis of key performance parameter extraction from current voltage measurements of photovoltaic devices. *Proceedings of the 37th IEEE Photovoltaic Specialists Conference* 2011; 002283–002288.
12. Emery KA, Osterwald CR. PV performance measurement algorithms, procedure and equipment. *Proceedings of the 21st IEEE Photovoltaic Specialists Conference* 1990; 1068–1073.
13. Standard test method for electrical performance of photovoltaic cells using reference cells under simulated sunlight. *ASTM International* 2009.
14. Emery K. Measurement and characterization of solar cells and modules. In *Handbook of Photovoltaic*



DOI: 10.1002/pip

*Science and Engineering*, Luque A, Hegedus S (edss), 2nd edn. John Wiley & Sons Ltd: Chichester, West Sussex, England, 2011; 701–752.

15. Paviet-Salomon B, Levrat J, Fakhfouri V, Pelet Y, Rebeaud N, Despeisse M, Ballif C. Accurate determination of photovoltaic cells and modules peak power from their current–voltage characteristics. *IEEE Journal of Photovoltaics* 2016; **6**(6): 1564–1575.
16. MATLAB Release 2012b. The MathWorks, Inc., Natick, Massachusetts, United States.
17. Bassi N, Clerc C, Pelet Y, Hiller J, Fakhfouri V, Droz C, Despeisse M, Levrat J, Faes A, Bätzner D, Papet P. GridTOUCH: innovative solution for accurate IV measurement of busbarless cells in production and laboratory environments. *Proceedings of the 29th European Photovoltaic Solar Energy Conference* 2014; 1180–1185.
18. Kojima H, Iwamoto K, Shimono A, Abe J, Hishikawa Y. Accurate and rapid measurement of high-capacitance PV cells and modules using a single short pulse light. *Proceedings of the 40th IEEE Photovoltaic Specialists Conference* 2014; 1896–1898.
19. Virtuani A, Rigamonti G. Performance testing of high-efficient highly-capacitive c-Si PV modules using slow-speed dark current–voltage characteristics and a reconstruction procedure. *Proceedings of the 28th European Photovoltaic Solar Energy Conference* 2013; 2876–2881.
20. Prorok M, Werner B, Zdanowicz T. Applicability of equivalent diode models to modeling various thin-film photovoltaic (PV) modules in a wide range of temperature and irradiance conditions. *Electron Technology* 2005; **37–38**(3): 1–4.
21. Merten J, Asensi JM, Voz C, Shah AV, Platz R, Andreu J. Improved equivalent circuit and analytical model for amorphous silicon solar cells and modules. *IEEE Transactions on Electron Devices* 1998; **45**(2): 423–429.
22. Unger EL, Hoke ET, Bailie CD, Nguyen WH, Bowring AR, Heumüller T, Christoforo MG, McGehee MD. Hysteresis and transient behavior in current–voltage measurements of hybrid-perovskite absorber solar cells. *Energy & Environmental Science* 2014; **7**: 3690–3698.